



On the spectral resolution of the broad-band indirect-geometry time-of-flight neutron spectrometer TOSCA

A. Perrichon

ISIS Facility, Rutherford Appleton Laboratory, Chilton, Didcot, Oxfordshire OX11 0QX, United Kingdom

ARTICLE INFO

Keywords:

TOSCA
Indirect-geometry spectrometer
Spectral resolution
Ray-tracing simulations

ABSTRACT

We present a detailed description of the spectral resolution of the TOSCA spectrometer at the ISIS Neutron and Muon Source. We compare an analytical model of the resolution, a numerical model based on ray-tracing simulations and experimental data derived from measurements of the 2,5-diiodothiophene standard. The analytical description is derived by error propagation on the energy transfer equation and accurately accounts for the dimensions of each of the component of the instrument and their neutron scattering or absorption depth-profiles. We obtain excellent agreement between the analytical and numerical descriptions for the ideal time-focusing geometry of TOSCA and also between the simulations of a more realistic model of the instrument and the experimental data. This study provides several insights into the critical contributions to the instrument performance that are directly useful for the proposed upgrade of TOSCA, but also relevant for other broad-band crystal-analyser spectrometers.

1. Introduction

The TOSCA spectrometer operated by the Molecular Spectroscopy Group at the ISIS Neutron and Muon Source (Harwell, U.K.) is a broad-band indirect-geometry time-of-flight (TOF) neutron spectrometer. It is optimised to measure with high energy resolution the spectral response of materials in the fingerprint region $\hbar\omega = 50\text{--}200\text{ meV}$ ($400\text{--}1600\text{ cm}^{-1}$), which is of particular importance to the study of molecular vibrations. As such, it can be considered as a chemical spectrometer that is the neutron analogue of infrared and Raman spectroscopies. TOSCA is active in many fields of research [1], including for instance catalysis [2], energy materials [3], advanced materials [4], or biological and organic compounds [5].

Other members of this family of chemical neutron spectrometers are the IN1 LAGRANGE spectrometer [6,7] at the Institut Laue Langevin (ILL; Grenoble, France), the VISION spectrometer [8] at the Spallation Neutron Source (SNS; Oak Ridge, TN, U.S.A.) and the NERA spectrometer [9] at the Frank Laboratory of Neutron Physics (FLNP; Dubna, Russia). All these instruments are indirect-geometry, crystal-analyser spectrometers, with VISION and TOSCA sharing a similar design.

Spectra measured on TOSCA are derived from measurements of the neutron time-of-flights. Neutrons generated at ISIS Target Station 1 (TS1) and moderated by a 300 K poisoned water moderator [10] are transported to the sample position in a supermirror neutron guide [11]. Neutrons scattered by the sample are analysed in energy by Bragg scattering on one of the ten modules of the secondary spectrometer. Each analyser module is constituted of a crystal analyser made of highly oriented pyrolytic graphite (HOPG) using the (002) reflection, a

cryo-cooled beryllium filter, and an array of 13 high-pressure (20 bar) squashed ^3He gas tubes. Besides suppressing higher order scattering from the analyser crystal, the beryllium filter suppresses the direct line-of-sight from sample-to-detector, which ensures a very low background in the detected signal. The scheme of the instrument geometry is shown in Fig. 1, reproduced from Ref. [12]. The notation used in this work is similar to that used to describe the geometry of the VISION spectrometer [8], and the coordinate system is based on the convention from the neutron ray-tracing simulations, with z along the instrument axis and x and y the radial directions in the horizontal and vertical planes, respectively.

The geometry of TOSCA secondary spectrometer (from sample to detector) is designed to achieve the best possible energy resolution in the fingerprint region by minimising the uncertainties in both the secondary TOF t_2 and the analysing energy E_2 . By having a flat crystal analyser and a flat detector array in the same plane as the sample, which gives near equal sample-to-analyser and analyser-to-detector distances ($L_{2a} \approx L_{2b}$ in Fig. 1), the variations of L_2 along the analyser are compensated by the variations of the scattering angle θ . This results in equal secondary TOF t_2 for each detector bin, regardless of the point of scattering on the analyser. This time-focusing effect thus minimises the uncertainties in t_2 by avoiding broadening due to spatial averaging on the detector, which is crucial as the helium tubes currently used on TOSCA are not position sensitive. The variations in scattering angle θ along the analyser however leads to a gradient of analysing energies E_2 on the detector along the y -direction. This gradient must be spatially resolved to minimise the uncertainties in E_2 , which explains the

E-mail address: adrien.perrichon@stfc.ac.uk.

<https://doi.org/10.1016/j.nima.2022.167401>

Received 4 July 2022; Received in revised form 9 August 2022; Accepted 22 August 2022

Available online 31 August 2022

0168-9002/© 2022 The Author(s). Published by Elsevier B.V. This is an open access article under the CC BY license

(<http://creativecommons.org/licenses/by/4.0/>).

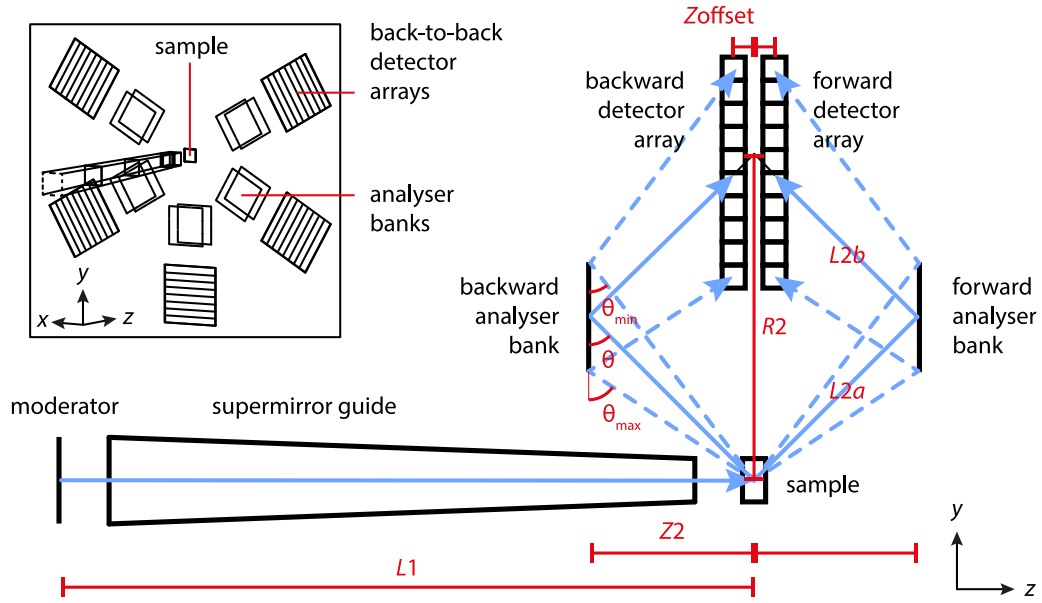


Fig. 1. Scheme of the TOSCA spectrometer reproduced from Ref. [12]. Not to scale. Components and optics in black, neutron paths in blue, geometric parameters in red. Only two back-to-back analyser modules are represented. Insert: Scheme of the TOSCA secondary including the ten analyser modules.

horizontal arrangement of the detector tubes (Fig. 1 insert). Besides time-focusing, TOSCA geometry also minimises the uncertainties in analysing energies that are due to the crystal mosaicity thanks to the prismatic effect of the HOPG tiles. Indeed, the geometry ensures that the energy gradient due to the variations of scattering angles along the analyser, and the energy gradient that is due to the range of neutron energies scattered by an infinitely small PG tile are identical. This results in an extended area of the analyser for which Bragg's law is fulfilled (the size of this region depends on the crystal mosaicity) that scatters neutrons of a specific energy towards a specific point on the detector array. This energy-focusing effect minimises the uncertainties in E_2 as long as the neutron image on the detector is vertically resolved. As a consequence of the time- and energy-focusing geometry of TOSCA, the resolution from the entire analyser is very similar to the resolution intrinsic to a single PG tile.

The parameters defining the instrument geometry are indicated in Fig. 1. Given the instrument geometry, the secondary flight path ($L_2 = L_{2a} + L_{2b}$) can be expressed from the normal distance between sample and analyser (Z_2) and the radial distance between the sample and the detector array (R_2). The scattering angle ranges from $\theta_{\min} = 41^\circ$ at the top of the analyser and $\theta_{\max} = 49^\circ$ at the bottom, with a value of 45° for the central tile of the analyser. The actual geometry of TOSCA deviates from the ideal time- and energy-focusing conditions due to the offset between the detector plane and the sample plane of $Z_{\text{offset}} \approx \pm 6$ cm, which leads to a minor degradation of the spectral resolution with respect to the ideal resolution.

TOSCA was upgraded in 2017 with the installation of a high- m supermirror guide that significantly increased the incident flux on the sample while maintaining the signal-to-noise ratio (SNR) and excellent spectral resolution of the instrument [11,13]. This enabled experiments that were previously borderline or impossible, such as molecules encapsulated in C_{60} or non-hydrogenous materials (SO_2 , CO, NO), allowed the measurement of much smaller samples, and facilitated parametric studies.

To capitalise on this successful upgrade and to further improve the detected intensity and SNR, an upgrade of the secondary spectrometer has been proposed as a part of the ISIS Facility Endeavour instrument upgrade program [12,14,15]. The key drivers are to increase the detected intensity by, mainly, increasing the coverage of the analyser (or solid angle), while maintaining the spectral resolution of TOSCA. The bulk of the design work is neutron ray-tracing (RT) simulations,

here performed with the McStas code [16–18], which is a numerical Monte Carlo method designed to efficiently propagate uncertainties and accurately calculate the performance the instrument, especially in terms of line shapes and resolution. The accuracy of RT simulations to properly describe the spectral resolution of spectrometers is generally excellent, with calculated values within 1%–10% error from the experimentally determined values, even when using simplified descriptions of the instruments. This is however not true when describing the TOSCA spectrometer, especially at high energy transfer where the “default” simulations severely underestimate the spectral resolution, as will be detailed hereafter.

To understand this discrepancy in the evaluation of the spectral resolution of TOSCA, we developed an analytical model of the spectral resolution, which we compare to experimental data and a new set of RT simulations. Compared to previous descriptions of this type of instruments [8,19–21], we use the formalism of expected values and variances to describe each component of the spectrometer (moderator, optics, sample, etc.) as distribution functions. We show that the main source of discrepancy originates from the evaluation of the secondary time-of-flight uncertainty, which is severely underestimated in the default description of the instrument with McStas. The correct evaluation of each individual contribution to the resolution is of particular importance in view of the proposed upgrade of the TOSCA secondary. Indeed, the strategy implemented in the design of neutron spectrometers usually consists of matching the resolution of the primary spectrometer (from source to sample), to that of the secondary spectrometer (from sample to detector), in order to achieve the best performance with respect to gain and resolution. This goal would be undermined by an incorrect evaluation of the secondary contribution. The precise description of the current TOSCA spectrometer, corroborated by the excellent agreement between the analytical and numerical descriptions, clearly highlights the opportunities for performance gains of the prospective upgrade.

Note that the analytical and numerical description proposed here are a development and correction of the authors' work in Ref. [12]. It differs in the analytical treatment of the crystal mosaicity, the modelling of the detector system and primary and secondary TOFs in both the analytical and numerical models.

2. Experimental resolution

The experimental spectral resolution of TOSCA has been derived from measurements of standards that can be considered near resolution-limited for neutron spectrometers, such as 2,5-diiodothiophene or Rb_2PtH_6 [22], and has been previously reported in Ref. [23].

An updated figure of the resolution after the installation of the neutron guide is produced from recent data of the 2,5-diiodothiophene standard. Below an energy transfer of $\hbar\omega = 150$ meV, the spectral bands exhibit an asymmetric tail and are better fitted with an exponentially-modified Gaussian (EMG) rather than a Gaussian function. Above 150 meV, the asymmetric tail is not observed, partly due to limited statistics and higher background levels, and the Gaussian and EMG fit agree equally well with the data. This is illustrated in Fig. 2 which shows the spectral bands at $\hbar\omega \approx 45$ meV (Fig. 2(a)) and ~ 150 meV (Fig. 2(b)) fitted with both Gaussian and EMG functions. While there are but minimal differences in the evaluation of the full width at half maximum (FWHM) between these two fitting approaches, the variance of the spectral bands is significantly different depending on whether an asymmetric tail is present or not. Indeed, ignoring the asymmetric tail leads to an underestimation of up to 50% of the variance for the most asymmetric spectral bands. The relation between peak shape and variance is further discussed hereafter for the moderator pulse shape.

We report in Fig. 2(c) the spectral resolution of TOSCA in the form of the FWHM's (estimated numerically from the best fitting function and divided by the incident energy E_1 assuming an average value of $E_2 = 3.65$ meV), in dependence on the energy transfer. The resolution is essentially identical to previous reports, with an average FWHM at the elastic line of 0.22(1) meV, which corresponds to 6.1(1)% of the average neutron incident energy. The best resolution is achieved in the energy range $\hbar\omega = 50$ –150 meV, with values of 1.2(2)% of the incident energy. Above 150 meV, the resolution increases to 2.2(1)% at $\hbar\omega = 380$ meV. We also report in Fig. 2(d) the standard deviation $\sigma(\hbar\omega)$ from the peak fit analysis (which includes the contribution of the asymmetric tail) as a function of energy transfer, which is later compared to the numerical model of the resolution.

3. Analytical description

3.1. Expressions of the energy transfer

Conceptually, the spectral resolution is the standard deviation or variance derived from the expression of the energy transfer, $\hbar\omega$. It follows that the resolution depends on all sources of uncertainties that affect the energy transfer, which are the uncertainties in the primary and secondary flight paths and TOFs. The energy transfer is expressed as:

$$\hbar\omega = E_1 - E_2, \quad (1)$$

where E_1 and E_2 are the neutron incident and final energy, respectively, which are derived from the time-of-flights according to:

$$E_1 = \frac{m_n}{2} v_1^2 = \frac{m_n}{2} \frac{L_1^2}{t_1^2} = \frac{m_n}{2} \frac{L_1^2}{(t - t_2)^2}, \quad (2)$$

$$E_2 = \frac{m_n}{2} v_2^2 = \frac{m_n}{2} \frac{L_2^2}{t_2^2}, \quad (3)$$

where m_n is the neutron mass and t the total time-of-flight measured at the detector. This then leads to the general expression of the energy transfer, which depends on the flight paths and time-of-flights:

$$\hbar\omega = \frac{m_n}{2} \left(\frac{L_1^2}{(t - t_2)^2} - \frac{L_2^2}{t_2^2} \right). \quad (4)$$

A similar expression, keeping E_2 instead of L_2 and t_2 , is used in the reduction process of TOSCA data to convert the spectra from TOF

to energy transfer. The values of t_2 , L_1 and E_2 are there empirically obtained for each detector bins by calibration to standards.

The expressions of E_2 and t_2 can be further developed by using Bragg's law, which leads to:

$$E_2 = \frac{h^2 n^2}{8m_n d_A^2} \csc^2(\theta), \quad (5)$$

$$t_2 = \frac{2m_n d_A}{hn} L_2 \sin(\theta), \quad (6)$$

where d_A is the interplanar spacing of the (002) reflection of pyrolytic graphite, $d_A = 3.354$ Å, h is the Planck constant, and n is the order of reflection. Substituting in Eq. (4), we obtain the expression for the energy transfer of crystal-analyser instruments:

$$\hbar\omega = \frac{m_n}{2} \frac{L_1^2}{\left(t - \frac{2m_n d_A}{hn} L_2 \sin \theta\right)^2} - \frac{h^2 n^2}{8m_n d_A^2} \csc^2(\theta). \quad (7)$$

Alternatively, we can use the specific geometry of TOSCA with the radial and normal distances R_2 and Z_2 to obtain:

$$E_2 = \frac{h^2 n^2}{8m_n d_A^2} \left[1 + \left(\frac{R_2}{2Z_2} \right)^2 \right], \quad (8)$$

$$t_2 = \frac{4m_n d_A}{hn} Z_2. \quad (9)$$

This latter notation shows explicitly that t_2 , given the geometry of TOSCA, only depends on the z -component of the secondary flight path, which is also true for the corresponding uncertainties. Substituting in Eq. (4), we obtain an expression for the energy transfer for the ideal TOSCA geometry:

$$\hbar\omega = \frac{m_n}{2} \frac{L_1^2}{\left(t - \frac{4m_n d_A}{hn} Z_2\right)^2} - \frac{h^2 n^2}{8m_n d_A^2} \left[1 + \left(\frac{R_2}{2Z_2} \right)^2 \right]. \quad (10)$$

Finally, we need to consider the impact of the mosaicity of the PG tiles on the final energy E_2 and on the secondary time-of-flight L_2 . In order to evaluate the effect on E_2 , we change formalism by replacing the scattering angle expressed as a scalar θ by a normal distribution of scattering angles, $\theta \sim \mathcal{N}(\mu, \sigma^2)$, characterised by its mean value (expected value), $\mu = E[\theta]$, and its variance, $\sigma^2 = V[\theta] = \eta^2/(8 \ln 2)$, where η is the crystal mosaicity. Based on Eq. (5), in order to obtain the mean value $E[E_2]$, we need to evaluate the mean value of $E[\csc^2(\theta)]$, which is easily done by using the complex notation forms of the trigonometric functions, as detailed in the Supporting Information (SI). Accordingly, and back in scalar notation, Eq. (5) can be developed into:

$$E_2 \approx \frac{h^2 n^2}{8m_n d_A^2} \frac{2}{1 - \cos(2\theta) \exp(-\eta^2/(4 \ln 2))}. \quad (11)$$

One can readily see that the contribution of the mosaicity to the value of E_2 is null for the specific case of $\theta = 45^\circ$, which corresponds to the central detector of TOSCA. At the top and bottom of the detector array, which correspond to scattering angles of 39° and 51° and mean final energies of 4.59 and 3.01 meV, respectively, the variations of the mean values of E_2 due to the mosaicity are -0.53 μeV at the top and $+0.1$ μeV at the bottom. The relative errors on the values of E_2 due to the mosaicity are thus less than 0.02%, which is negligible.

Note that Eq. (11) predicts, in backscattering condition with $\theta = 90^\circ$, that the average value of E_2 is slightly increased due to the mosaicity. This result may appear counter-intuitive since $dE_2/d\theta = 0$ for $\theta = 90^\circ$. However, because variations of the scattering plane angle in any direction due to the mosaicity always decrease the scattering angle from perfect backscattering condition, then the average value of E_2 is necessarily increased when the mosaicity is accounted for, even though the effect is minor. The absence of effect of the mosaicity at $\theta = 45^\circ$ is due to the contribution of the planes tilted in $(\theta - \epsilon)$ exactly compensating the contribution of the planes tilted in $(\theta + \epsilon)$, at the special scattering angle of $\theta = 45^\circ$ at which $\cos(2\theta)$ changes sign.

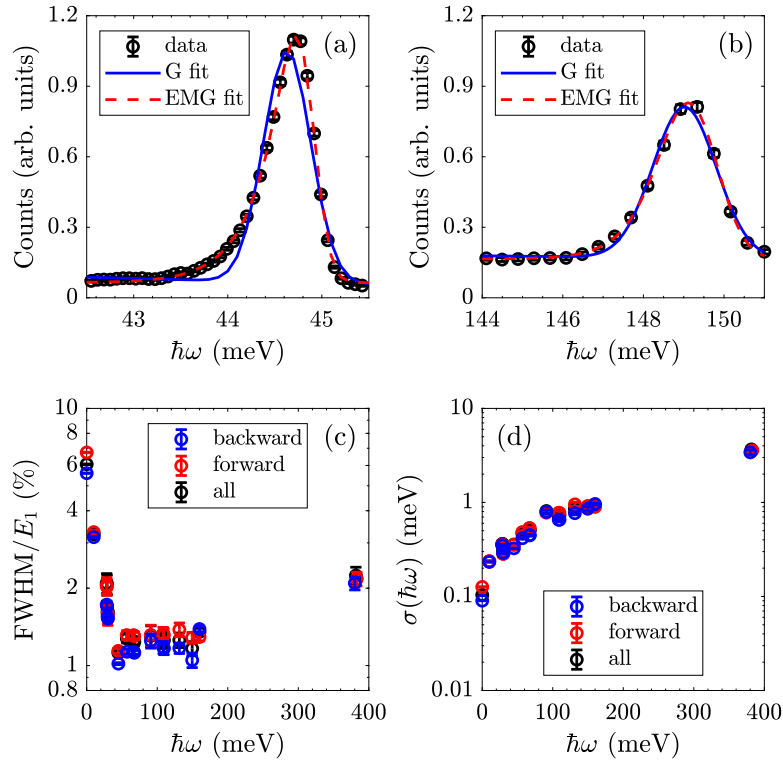


Fig. 2. Experimental data of the 2,5-diiodothiophene standard, averaged over all detectors: spectral bands at (a) $\hbar\omega \approx 45$ meV and (b) ~ 150 meV, fitted with a Gaussian (G) function and flat background (full blue line), and exponentially-modified Gaussian (EMG) function and a flat background (dashed red line). Spectral resolution of TOSCA of the backward detector banks only, forward detector banks only, and all detector banks, (c) expressed as FWHM/E_1 in % and (d) as standard deviation $\sigma(\hbar\omega)$ in meV that accounts for the asymmetric peak shape. The spread in fitted values in panels (c) and (d) is mainly due to difficulties in assessing local backgrounds in the experimental spectra.

Regarding the effect of the mosaicity on the secondary flight path L_2 , because of the energy-focusing principle, we only need to consider the variations of paths to a specific arrival point on the detector, i.e., all the neutrons scattered on an extended region of the analyser that reach the same detector bin. This effect is schematised in Fig. 3, which shows a tile that is tilted by an angle ϕ and offset by a distance ξ vertically (in red), and tilted by an angle ψ and offset by a distance ζ horizontally (in yellow), while scattering the neutron towards the same point on the detector as an ideal tile (in blue). Here ϕ and ψ are random values from the normal distribution of scattering angle due to the vertical and horizontal mosaicity.

Starting with the vertical mosaicity in Fig. 3(a), the dependency of ϕ on the secondary flight path L_2 projected in (yz) can be expressed as:

$$L_2^{yz}(\phi) = L_{2a}(\phi) + L_{2b}(\phi), \quad (12)$$

$$= Z_2 \left[\csc(\theta - \phi) + \csc(\theta + \phi) \right], \quad (13)$$

$$\approx 2Z_2 \csc(\theta). \quad (14)$$

It follows that, for the ideal TOSCA geometry, in the approximation of infinitely thin detector pixels and for reasonably small values of ϕ , L_2 is independent of the vertical mosaicity as intended by the application of the energy-focusing principle. For the horizontal mosaicity in Fig. 3(b), L_2 projected in (xz) is:

$$L_2^{xz}(\psi) = L_{2a}(\psi) + L_{2b}(\psi), \quad (15)$$

$$= 2Z_2 \sec(\psi). \quad (16)$$

It follows that the impact of the horizontal mosaicity is negligible, since $\sec(\psi) \approx 1$ for small values of ψ . The total, 3-dimensional expression of L_2 for a PG tile tilted by (ϕ, ψ) is then:

$$L_2(\phi, \psi) \approx 2Z_2 \csc(\theta) \sec(\psi). \quad (17)$$

In order to obtain the mean value of L_2 , we need to evaluate the expected values $E[\csc(\theta)]$ and $E[\sec(\psi)]$, which is done by changing the formalism as previously shown for the final energy. Details are in the Supporting Information, and the result, in scalar notation and assuming equal mosaicity in the vertical and horizontal directions, is simply:

$$L_2 \approx 2Z_2 \csc(\theta) \exp\left(\frac{\eta^2}{8 \ln 2}\right). \quad (18)$$

This shows that the mean value of L_2 is slightly increased when the mosaicity is included, although the effect is negligible. Since we have shown that, for the ideal TOSCA geometry, the effect of the mosaicity on the neutron final energy and secondary flight path are negligible, we will ignore the mosaicity entirely in the analytical description and use the general expression of the energy transfer (Eq. (4)) that solely focuses on flight paths and time-of-flights, keeping in mind that for the ideal TOSCA geometry, the uncertainties in t_2 only depends on the z -component of the uncertainties in L_2 (Eq. (9)).

However, this approximation only holds for the ideal geometry, with the pixel size on the detector system considered infinitely thin and with the detector array laying exactly in the sample plane. Note that both effects slightly degrade the resolution. The impact of the detector pixel size is not treated here, but is extensively discussed for the VESPA instrument by Zanetti et al. in Ref. [14]. The impact of the offset distance between the sample and detector planes (Z_{offset}) is evaluated hereafter in the numerical description of the resolution.

3.2. Error propagation

The variance representing the resolution function, now referred to as $V[\hbar\omega]$, is calculated by error propagation of the general expression of the energy transfer (Eq. (4)), assuming that the variables are independent, according to:

$$V[\hbar\omega] \approx \left(\frac{\partial \hbar\omega}{\partial t}\right)^2 V[t] + \left(\frac{\partial \hbar\omega}{\partial t_2}\right)^2 V[t_2] \dots \quad (19)$$

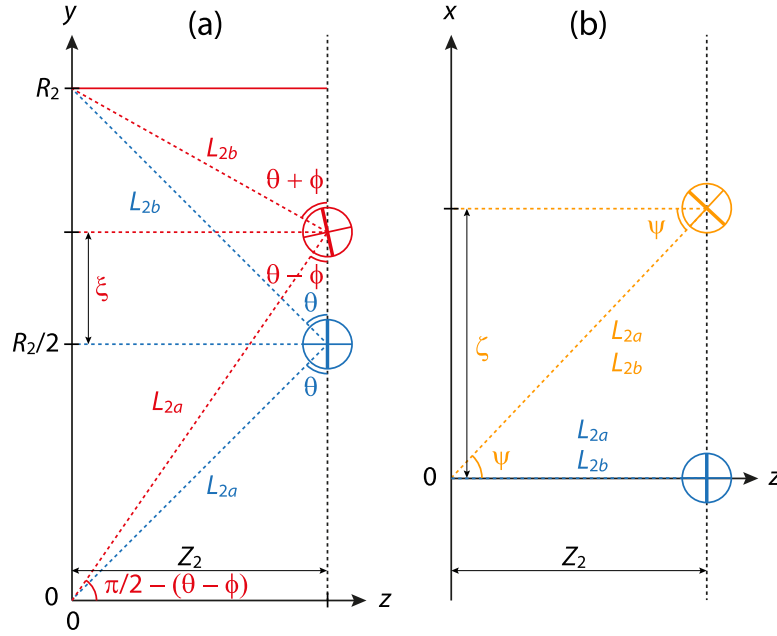


Fig. 3. Scheme of the geometric relations between the angles ϕ and ψ and the tile displacements ξ and ζ .
Source: Reproduced and adapted from Ref. [12].

$$+ \left(\frac{\partial \hbar \omega}{\partial L_1} \right)^2 V[L_1] + \left(\frac{\partial \hbar \omega}{\partial L_2} \right)^2 V[L_2].$$

Here we chose the error propagation method over the total differential method used for VISION in [8] and previously for TOSCA in [19] for its higher degree of precision, and the variance formalism over the standard deviation formalism, as it is convenient to describe distributions. The squared partial derivatives are expressed as follow:

$$\left(\frac{\partial \hbar \omega}{\partial t} \right)^2 = \frac{m_n^2 L_1^4}{(t - t_2)^6}, \quad (20)$$

$$\left(\frac{\partial \hbar \omega}{\partial t_2} \right)^2 = \frac{m_n^2 L_1^4}{(t - t_2)^6} + \frac{m_n^2 L_2^4}{t_2^6} + \frac{2m_n^2 L_1^2 L_2^2}{(t - t_2)^3 t_2^3}, \quad (21)$$

$$\left(\frac{\partial \hbar \omega}{\partial L_1} \right)^2 = \frac{m_n^2 L_1^2}{(t - t_2)^4}, \quad (22)$$

$$\left(\frac{\partial \hbar \omega}{\partial L_2} \right)^2 = \frac{m_n^2 L_2^2}{t_2^4}. \quad (23)$$

Note that when we consider distributions instead of scalars, we have to evaluate individually all powers since $E[x^n] \neq (E[x])^n$. While the evaluation of the power 2 is simple with the variance definition stating $E[x^2] = (E[x])^2 + V[x]$, at higher power for $n > 2$ the expression of $E[x^n]$ depends on the shape of the distribution.

We report in Table 1 the 1-dimensional (1D) distributions that can be used to describe the different components of the TOSCA spectrometer, including the expression of their variance based on their characteristic parameters. Considering that the point of exit of the neutron on the moderator surface is not correlated to the point of arrival on the sample, we can describe the 3 dimensions of the moderator by rectangular distributions. The moderator face is 120 mm wide and 115 mm tall, and is tilted by 13.2° from the instrument z -axis. This gives variances of ~ 1137 , 1102 and 63 mm^2 for the moderator in the x -, y -, and z -directions, respectively.

We consider a sample size of $40 \times 40 \times 1 \text{ mm}^3$ that corresponds to the standard flat cells commonly used on TOSCA. The sample is described by rectangular distributions in the x - and y -directions. In the approximation that the sample is weakly scattering, we also consider a rectangular distribution in the z -direction. This gives variances of $\sim 133 \text{ mm}^2$ in the x - and y -directions, and $\sim 0.08 \text{ mm}^2$ in the z -direction.

The analyser is considered perfect and the secondary flight path expected values and uncertainty are calculated from the sample and detector only, since we have shown that for the ideal time-focusing geometry the PG crystal mosaicity plays a negligible role. The contribution of the PG tile thickness is evaluated hereafter in the numerical simulations.

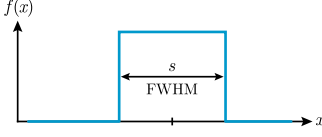
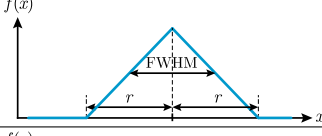
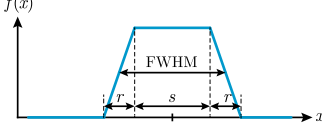
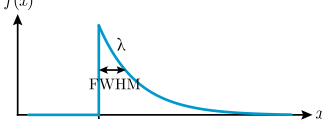
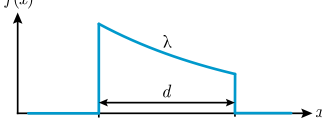
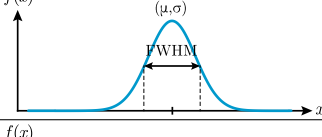
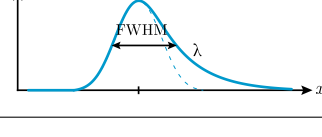
The squashed detector can be approximated by rectangular distributions in the x - and y -directions. For simplicity, we consider a bank aligned along the y -axis in the description, for instance the bottom forward bank. The detector height of 14.5 mm and width of 188 mm give variances of $\sim 18 \text{ mm}^2$ and 2945 mm^2 , for the y - and x -directions, respectively, if we consider rectangular distributions. However, because of the collimation imposed by the built-in cadmium blades of the beryllium filter (described in detail hereafter), we can instead consider that the distribution is triangular in the x -direction (from the distribution of intensity on the detector). With a divergence cut-off from the linear collimation of $\sim 14^\circ$ and $Z_2 = 220 \text{ mm}$, the detector image is characterised by a half-width $r \approx 112 \text{ mm}$, which gives a variance of $\sim 2104 \text{ mm}^2$. The detector z -direction is the most complex and illustrates well the importance of the choice of the distribution. Let us consider neutrons with an energy of 3.65 meV that intercept the detector surface at an angle of 45° . As a first approximation, we model the squashed detector of TOSCA as infinite in (x, y) and with a thickness in z of 2.54 mm. The maximum path length of the neutron in ^3He is thus $2.54/\cos(45) \approx 3.59 \text{ mm}$. If we consider that the capture profile is uniform, the variance would be $(3.59)^2/12 \approx 1.08 \text{ mm}^2$. If we ignore the path length and solely consider an exponential decay with a decay constant:

$$\lambda = \frac{P \sigma_{\text{abs}}}{k_B T} \approx 0.678 \text{ mm}^{-1}, \quad (24)$$

where P is the ^3He pressure of 20 bar, k_B is the Boltzmann constant, $T = 300 \text{ K}$ the detector temperature, and σ_{abs} the absorption cross section of ^3He , then the variance would be $\sim 2.18 \text{ mm}^2$. Finally, if we consider a truncated exponential decay distribution, using the previously calculated value of λ and a cut-off at the maximum path length, then the variance is $\sim 0.82 \text{ mm}^2$. The variance is thus very dependent on the choice of the distributions used to describe the scattering or absorption profiles.

Table 1

Distributions (1D) that can be used to describe the components of the TOSCA spectrometer, with the expressions for their variance V and full width at half maximum (FWHM) when applicable.

Distribution	Scheme	Variance	Used for: (dimension) component
Rectangular [24]		$V = \frac{s^2}{12} = \frac{\text{FWHM}^2}{12}$	(x, y, z) moderator, (x, y) sample, (z) sample if weak scatterer, (y) detector
Isosceles triangular [24]		$V = \frac{s^2}{6} = \frac{\text{FWHM}^2}{6}$	(x) detector, due to linear horizontal collimation
Isosceles trapezoid [24]		$V = \frac{(2r^2 + 2rs + s^2)}{12}$ $= \frac{(\text{FWHM}^2 + r^2)}{12}$	1D distances, combination of two rectangular distributions
Exponential decay		$V = \frac{1}{\lambda^2} = \frac{\text{FWHM}^2}{\ln(2)^2}$	neutron capture or scattering profiles, (z) detector, if close to 100% efficiency
Truncated exponential decay [25]		$V = \frac{1}{\lambda^2} - \frac{d^2 \exp(\lambda d)}{(\exp(\lambda d) - 1)^2}$	neutron capture or scattering profiles, (z) sample, if strong scatterer, (z) detector
Normal distribution		$V = \sigma^2 = \frac{\text{FWHM}^2}{8 \ln(2)}$	Symmetric description: (r) moderator, (ho) peak shape
Exponentially modified Gaussian (EMG) [26]		$V = \sigma^2 + \frac{1}{\lambda^2}$	Skewed description: (r) moderator, (ho) peak shape

Similarly, details of the exact geometry of the optics and components constituting the spectrometer are critical for the correct evaluation of the uncertainties. For instance, instead of the simplified model of an infinite detector, we now consider the exact dimensions of the squashed tubes and their assembly, which is rectangles with semicircles at a pair of opposite sides (stadiums) of outer dimensions defined by a radius $r = 2.54/2$ mm and a length $a = 12.96$ mm, with wall thicknesses of 200 μm and a separation between adjacent stadiums of 200 μm , as represented in Fig. 4(a). We can then evaluate the maximum path length, thus the variance, as a function of the position along the detector array (Fig. 4(b)). The average variance from the neutron capture profile, including geometric effects, is then $\sim 0.56 \text{ mm}^2$, which is a factor 2 lower than the initial evaluation with a uniform distribution.

3.3. Expected values of a distribution of distances

Now that the components of the spectrometer (moderator, sample, detector) have been described with 1D distributions, we are interested in the expression of the distribution of distance between two of these 3-dimensional (3D) components, to derive the expected values at various powers of the primary and secondary flight paths.

The estimated value of the squared distance D^2 between two 3D objects is straightforwardly obtained from the squared Euclidean distance, according to:

$$E[D^2] = E[X^2] + E[Y^2] + E[Z^2], \quad (25)$$

with X , Y and Z the distance distributions in the x , y and z directions, respectively. The variance $V[D]$ is obtained by error propagation of the Euclidean distance, which leads to:

$$V[D] = \frac{E[X^2]V[X] + E[Y^2]V[Y] + E[Z^2]V[Z]}{E[X^2] + E[Y^2] + E[Z^2]}. \quad (26)$$

Using the variance definition in Eqs. (25) and (26), the distribution of distance D develops into:

$$E[D] = \left\{ E[X]^2 + E[Y]^2 + E[Z]^2 + \frac{V[X](E[Y^2] + E[Z^2])}{E[X^2] + E[Y^2] + E[Z^2]} + \frac{V[Y](E[X^2] + E[Z^2])}{E[X^2] + E[Y^2] + E[Z^2]} + \frac{V[Z](E[X^2] + E[Y^2])}{E[X^2] + E[Y^2] + E[Z^2]} \right\}^{\frac{1}{2}}. \quad (27)$$

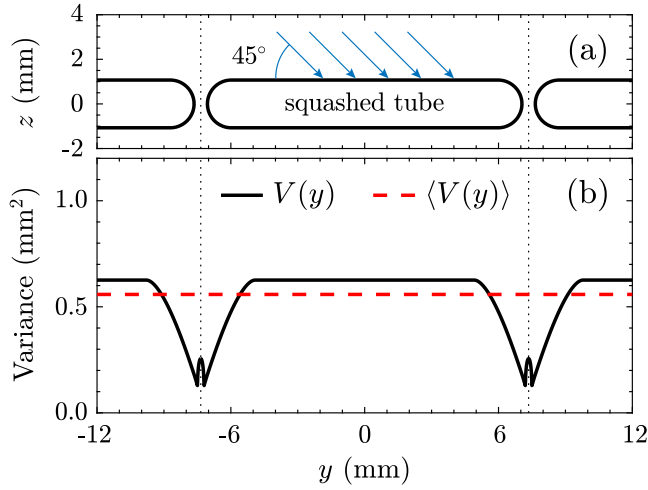


Fig. 4. (a) Scheme of adjacent squashed detector tubes approximated by stadiums. The incident neutrons are represented by blue arrows. The neutron incidence angle is 45° from the detector plane. (b) Variance calculated assuming a truncated exponential decay for the neutron capture, with a cut-off value corresponding to the maximum path length at the position y along the detector array (black line), and its average (dashed red line).

This shows that a distance between two 3D objects with finite dimensions is necessarily higher than the distance between two point-objects. Note that, given the dimensions of the components and the distances between them, the difference between point-geometry values and the results from Eq. (27) is only about 2 mm for L_2 (< 1%) and is negligible for L_1 .

The next step is to express the expected values and variances of the 1D distributions of distances X , Y and Z used in Eq. (27). Regardless of the shape of the distributions of the two 1D objects, the distance is simply obtained from the position of the means (centre-of-mass for a rectangular object, $1/\lambda$ from the surface for an exponential decay). Similarly, since each component is independent, the variance of the distance is simply the sum of the variance of each component's dimensions.

In the case where components' dimensions are large with respect to their distance, which may only be relevant for L_2 here, then expressions for the higher powers of $E[X^n]$ beyond $n > 2$ are needed. This requires information on the shape of the convolution of the 1D distributions describing the two objects. The problem can be solved exactly when the two components can be described by rectangular distributions (e.g. rectangular sample and detector array for the y -component of L_2), as their convolution leads to an isosceles trapezoidal distribution, for which the variance and expected values at any power are known analytically [24]. The expressions of the distance between two rectangular objects, up to the power 6, are reported in the Supporting Information.

This approach is different from the one developed for VISION [8]. We here consider that L_1 and L_2 are 3D vectors connecting two 3D objects, while the work on VISION considers only the z -component of L_1 and splits L_2 into Z_2 (1D) and R_2 (2D). The two approaches differ for R_2 and Z_2 .

Let us consider an analyser arm oriented horizontally along the x -axis, with a value of R_2 of 440 mm, a rectangular sample with dimensions along x and y of $\Delta X_S = \Delta Y_S = 40$ mm, and rectangular detector with dimensions along x and y of $\Delta X_D = 14.5$ mm and $\Delta Y_D = 188$ mm, respectively. According to Ref. [8], the simplified expression of $V[R_2]$ is:

$$V[R_2] = \frac{\Delta X_D^2 + \Delta X_S^2}{12} + \frac{\Delta Y_D^4}{720R_2^2}. \quad (28)$$

This gives a variance in R_2 of ~ 151 mm² (standard deviation of ~ 12.3 mm). In comparison, with the same example in 2D, Eq. (26)

develops into:

$$V[R_2] = \frac{E[X]^2 V[X] + V[X]^2 + V[Y]^2}{E[X]^2 + V[X] + V[Y]}, \quad (29)$$

where $E[X]^2 = 440^2$ mm², and $V[X]$ is the sum of the variances of the two objects in the x -direction (idem for $V[Y]$ in the y -direction):

$$V[X] = \frac{40^2}{12} + \frac{14.5^2}{12}, \quad (30)$$

$$V[Y] = \frac{40^2}{12} + \frac{188^2}{12}. \quad (31)$$

This gives a variance in R_2 of ~ 197 mm² (std of ~ 14.0 mm). The simplified version of Eq. (29) with similar assumptions to those in Ref. [8], which is considering point-geometry distances and that $V[Y] \gg V[X]$, would be:

$$V[R_2] \approx V[X] + \frac{V[Y]^2}{E[X]^2}, \quad (32)$$

which looks akin to Eq. (28) and gives $V[R_2] \approx 200$ mm² (std of 14.1 mm). Note that the approach developed here with Eq. (26) is robust as it accounts for all dimensions, any orientation of the distance vector between the two objects, and does not make any assumptions about the shape of the distributions describing the objects. It follows that it is unnecessary to consider a trapezoid distribution to describe R_2 and calculate its variance, as done in Ref. [8]. Note though that it is not incorrect, as hinted by the similar forms of the variances in the x -directions in Eqs. (28) and (30). Indeed, the variance of an isosceles trapezoid is simply the sum of the variance of the two convoluted rectangular functions, which is equivalent to the general case of two independent distributions.

3.4. Moderator pulse shape

The moderator pulse shape is formally described by an Ikeda-Carpenter distribution [27]. However, the analytical mean and variance of this function is non-trivial, and instead a common approximation is to use a normal distribution, though this approach neglects the asymmetric tail of the pulse. By instead using an exponentially-modified Gaussian distribution (EMG) [26], the moderator pulse shape can be described for various degrees of asymmetry. The analytical variance of the EMG is reported in Table 1. Depending on the degree of asymmetry, the variance can either be dominated by the Gaussian term σ^2 or the exponential decay term $1/\lambda^2$.

The variance of the moderator pulse shape is obtained by fitting a numerical model of the TOSCA moderator designed by the ISIS Neutronics group (the same file is later used for the numerical simulations). Fig. 5 panels (a)–(c) shows the TOF at moderator surface for several energy transfer $\hbar\omega$. We also report in Fig. 5 the fit of the TOF using the Ikeda-Carpenter, Gaussian, and EMG models. While the EMG cannot fully reproduce the pronounced asymmetry in the 50–100 meV range, the agreement to the TOF is far better than with the Ikeda-Carpenter and Gaussian models for all energy transfers.

The variances from the Gaussian and EMG fits of the TOF at moderator surface in dependence of the energy transfer $\hbar\omega$ are shown in Fig. 5(d). The variance from the EMG fit is of the order of ~ 340 μs^2 at the elastic line, then progressively decreases and, for instance, takes values of ~ 145 μs^2 at $\hbar\omega = 50$ meV, ~ 40 μs^2 at $\hbar\omega = 100$ meV, and ~ 15 μs^2 at $\hbar\omega = 150$ meV. It is clear in Fig. 5(d) that using a Gaussian model systematically underestimates the variance of the TOF distribution, compared to the EMG model. It is also apparent that, for TOSCA, the variance from the pulse shape is dominated for all energy transfers by the exponential decay term. Note though that, if only the FWHM is of interest, i.e. if only the pulse width is considered as a source of uncertainty, the Gaussian model still gives an acceptable estimate.

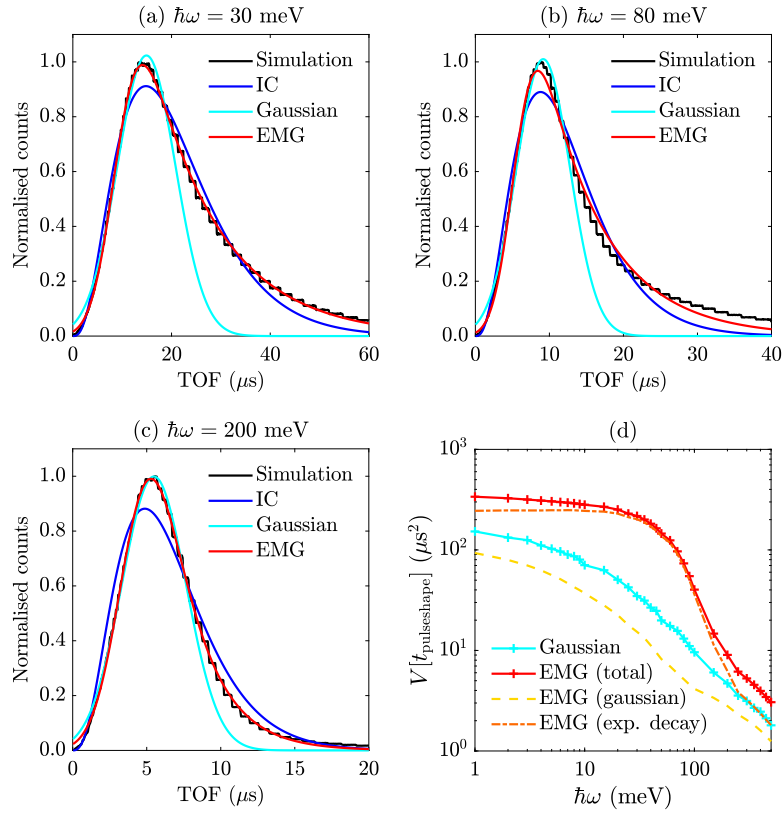


Fig. 5. TOF at moderator for (a) $\hbar\omega = 30$ meV, (b) $\hbar\omega = 80$ meV, and (c) $\hbar\omega = 200$ meV. The corresponding incident energies are in the range $[\hbar\omega + 2.5, \hbar\omega + 5.5]$ meV. Simulated TOF from numerical model (black lines) and fits with Ikeda-Carpenter (IC, blue lines), Gaussian (cyan lines) and EMG (red lines). Note that the Gaussian function is fitted on the limited TOF interval $[0, \mu + \sigma\sqrt{2\ln 2}]$. (d) Variance in μs^2 of the Gaussian and EMG models.

3.5. Uncertainties in time

Beyond the variance originating from the moderator pulse shape, other sources of uncertainties in time are present that affect the secondary TOF. These are the time binning scheme of the detector acquisition electronic (DAE) system, and the time resolution intrinsic to the detector geometry and electronics. The time binning scheme on TOSCA is uniform with a time bin of 4 μs . This corresponds to a rectangular function with variance $V = 4^2/12 \approx 1.3 \mu s^2$. Compared to the other sources of uncertainty, this contribution only has a minor effect at high-energy transfer.

The detector time resolution is linked to the distribution in the delay between the neutron capture event by ^3He in the detector tube and the timestamp of this event by the electronics. This depends on the kinematics of the reaction process and the time constant used for charge collection as well as the ability of the electronics to identify the peak maximum. For a ^3He cylindrical tube with recent electronics, the time resolution (standard deviation) is estimated to be 1 μs . In the case of the squashed tubes exploited on TOSCA, the electric field is heterogeneous, especially by the stadium extremities, and the detected signal should exhibit an asymmetric profile with a tail towards long time. This effect, combined with the ageing electronics, leads to a degraded time resolution estimated to be $\sim 10 \mu s$, thus a large variance of $\sim 100 \mu s^2$ (ISIS Detector group, personal communication, March 2022). The detector time resolution is thus a significant contribution to the spectral resolution at high energy transfer and becomes the main source of uncertainty in time, in front of the moderator pulse shape, for $\hbar\omega > 70$ meV. This also means that an upgrade of the detector system that lowers the contribution of the detector time resolution to 1 μs would significantly improve the spectral resolution at high-energy transfer.

Besides the time binning scheme and detector time resolution, the other source of uncertainty in t_2 is linked to the neutron path that

cannot be resolved by the detector, which in first approximation is the z -component of L_2 . In the ideal time-focusing geometry, the expected value and variance of t_2 are derived by error propagation on Eq. (9), which gives:

$$V[t_2] = \frac{16m_n^2 d_A^2}{h^2 n^2} V[Z_2] = \frac{4m_n^2 d_A^2}{h^2 n^2} V[L_2(z)]. \quad (33)$$

The contributors to $V[L_2(z)]$ are the sample thickness, the tile thickness and the detector capture profile along z . A 1 mm thick, weakly scattering sample modelled by a rectangular distribution has a variance of $1^2/12 \approx 0.08 \text{ mm}^2$. We have shown in the previous section that the variance from the neutron capture profile in the detector is $\sim 0.56 \text{ mm}^2$ when the detector stadium geometry is accounted for. With the same approach, if we consider only the z -component of the neutron path in the detector, we obtain a variance of $\sim 0.31 \text{ mm}^2$. The contribution of the tile thickness is complex to evaluate due to multiple scattering effects from the strong scattering by the (002) plane of PG and will be evaluated in the numerical simulations.

In the ideal scenario where the tile thickness does not contribute, Eq. (33) gives a value of $\sim 1.12 \mu s^2$, which is negligible in comparison to the other contributions. Note that this contribution is so low because of the ideal time-focusing geometry of TOSCA, which imposes a uniform front of neutron arrival times on the detector regardless of their point of scattering on the analyser, so that only the z -component of the secondary flight path uncertainty impacts the secondary TOF uncertainty. The uncertainty in t_2 might become significant when large curved analysers that deviate from the ideal time-focusing geometry are implemented as proposed for the TOSCA secondary upgrade, as part of the much larger variances in the x - and y -direction (especially from the sample height) may then contribute. The value calculated for the ideal geometry is then the baseline value of $V[t_2]$ given by the distributions of neutrons in the sample, tile and detector. To get the best possible resolution at high energy transfer, the optimisation

strategy of the design of large curved analysers should then be focused on minimising the variance in t_2 to obtain a value as close as possible to the baseline.

As for the flight paths, there are differences with the approaches implemented here and for VISION [8] to evaluate the secondary time-of-flight. While the relationship of Eq. (33) to obtain $V[t_2]$ from $V[Z_2]$ or $V[L_2(z)]$ is essentially identical, the work on VISION sums the standard deviations from the sample, tile, and detector thicknesses, while here we consider the sum of the variances. Indeed, from Ref. [8], the standard deviation of the secondary TOF, $\sigma[t_2]$, is:

$$\sigma[t_2] = \frac{2m_n d_A}{h} (\sigma_{\text{sample}} + 2\sigma_{\text{tile}} + \sigma_{\text{detector}}), \quad (34)$$

where σ_{tile} is evaluated from numerical simulations to give $\sigma_{\text{tile}} = 0.7$ mm and σ_{sample} and σ_{detector} are calculated analytically by considering rectangular distributions for the z -direction of the sample and detector, which gives $\sigma_{\text{sample}} \approx 0.58$ mm and $\sigma_{\text{detector}} \approx 0.87$ mm for a 2 mm thick sample and 3 mm thick detector, respectively. This gives $\sigma[t_2] \approx 4.82$ μs thus a variance in t_2 of ~ 23.2 μs^2 . With the same values for the standard deviations of the sample, tile and detector, the variance calculated with Eq. (33) is ~ 4.5 μs^2 , about a factor 5 lower than from Eq. (34). The fundamental difference is that the sources of uncertainties in t_2 are considered fully correlated in Ref. [8], while they are considered independent in the present work. Because the dependency of the resolution with the scattering angle is suppressed in the ideal time- and energy-focusing geometry, we consider that the time delays accumulated by the neutron in the sample, analyser and detector are uncorrelated.

4. Numerical description

4.1. The McStas instrument

The numerical simulations of the instrument were performed with the Monte Carlo ray-tracing package McStas version 2.7.1 [16,17,28], operated with an in-house Matlab code. The spectrometer is described by a sequence of components, from moderator to detector, along which the neutron rays propagate. The 300 K poisoned moderator seen by TOSCA is modelled with the *Commodus.I* component linked to the external moderator file *TS1verBase2016_LH8020_newVM-var_North08_Tosca* produced by the ISIS Neutronics group. The component represents a 12×11.5 cm^2 source that direction focuses neutrons towards a 10×10 cm^2 surface located 1.626 m away, at the entrance of the guide. To improve statistics we also use energy focusing, limiting the neutron energies to the targeted energy transfer, $[\hbar\omega + 2.5, \hbar\omega + 5.5]$ meV. Note that this component includes the tilt of the moderator surface with respect to the instrument axis.

The guide is constituted of ten straight sections, modelled with ten instances of the *Guide* component. The guide dimensions and reflectivities are based on the model by Pinna et al. and we obtain here identical beam and divergence profiles as reported in Ref. [11], which also contains the detailed description of the guide.

The *Incoherent* component is used to describe the typical elastic or inelastic incoherent scattering sample of TOSCA. The component is set to represent a large 40×40 mm^2 flat cell with a thickness of 1 mm. The incoherent and absorption cross sections are fixed to the values of vanadium. To scan in energy, we use the “Etrans” parameter, which shifts the elastic line by an energy $\hbar\omega$ (same parameter as for the moderator). Multiple scattering by the sample is not accounted for as it is not part of the instrument performance. We use direction focusing to improve statistics by targeting the PG analyser.

The PG analyser is modelled here with two components. In first approximation we use the *Monochromator_curved* component, which represents an infinitely thin mosaic crystal with a single scattering vector normal to the surface. This component ignores entirely the contribution of the PG tile to the uncertainty in t_2 . Parameters defining the material are the d -spacing of 3.354 Å and the mosaicity of 120

arcmin. Alternatively, the PG tile is modelled with the *Single_crystal* component using the reflection list “C_graphite.lau” and the lattice matrix $[0, 2.14, -1.25; 0, 0, 2.47; 6.71, 0, 0]$. In that case the tile thickness is set to 2 mm. Note that while the PG tile now contributes to the uncertainty in t_2 , as the neutron actually penetrates inside the tile, the *Single_crystal* component is but a coarse model. The trapezoid shape of the PG analyser is reproduced using 92 tiles of individual dimensions 12×12 mm^2 , which gives the correct analyser surface of 132.5 cm^2 . Only one of the ten arms of the instrument is simulated at a time.

The beryllium filter is not modelled with McStas but its effects are accounted for in post-processing, as described afterwards.

Finally neutrons are monitored at the surface of the detector array, and the individual neutron states are stored in event mode using the *Monitor_nD* component. Note that, besides the neutron position, velocity, energy and TOF, we also record the TOF that the neutron had when scattered by the sample, which allows us to calculate the exact values of t_2 and L_2 . The effects of neutron propagation in the detector are accounted for in the post-processing. The position of the monitor with respect to the sample plane is in the ideal case $Z_{\text{offset}} = 0$, while a more realistic evaluation uses $Z_{\text{offset}} = 59$ mm (see Fig. 1).

4.2. Post-processing of the McStas simulations

Post-processing accounts for the effects of the beryllium filter and gas detectors on the neutron transport. The beryllium filter is an assembly of beryllium wedges each separated by neutron absorbing blades in cadmium. The primary function of the beryllium filter is to suppress high energy neutrons reaching the detector due to higher-order scattering from pyrolytic graphite. Its secondary function, due to its positioning between the analyser and detector and the presence of cadmium blades and shielding, is to suppress the direct line-of-sight between sample and detector and block stray neutrons scattered by the sample environment and analyser back plate. Because the collimation imposed by the cadmium blades impacts the neutron distribution on the detector, its impact on the resolution should be estimated. However, the high energy neutrons filtering performance of the beryllium filter have no impact on the resolution, as transmitted neutrons do not interact with the filter. Consequently, we choose here to only consider the collimation imposed by the cadmium blades. The cadmium blades are rectangular, 12 cm long, 10 cm tall with a thickness of 1 mm. They are parallel to each other and separated by 3 cm of beryllium, thus resulting in a linear horizontal collimation with a triangular transmission profile that has an associated divergence cut-off $\tan^{-1}(3/12) \approx 14^\circ$. In first approximation, this triangular transmission can be accounted for analytically by scaling the weight of the neutron rays reaching the monitor based on their horizontal divergence.

Alternatively, we can consider the physical presence of the blades and assess for each neutron ray if their trajectory collides with a blade. While this numerical option is computationally expensive, it accurately accounts for the shadows cast by the cadmium blades onto the detector. We show in Fig. 6 a PSD-picture of the distribution of intensity at the detector position without the collimation (Fig. 6(a)), and for the analytical (Fig. 6(b)) and numerical (Fig. 6(c)) evaluations of the collimation. Compared to the case without collimation, the relative average transmission of analysed neutrons is 51% and 45% for the analytical and numerical models, respectively. These low transmission values are due to the mismatch between the horizontally diverging neutron beam scattered by the flat analyser and the linear horizontal collimation imposed by the filter, which suppress most neutrons scattered at the analyser sides. Note that the current filter was obtained by machining the rectangular monoliths of beryllium previously used on the instrument. Despite its low transmission compared to today’s standards, the addition of cadmium blades led to a significant improvement of the SNR [23].

As shown by the disparities in transmission between the two models of the collimation, accurately accounting for the cadmium blades with

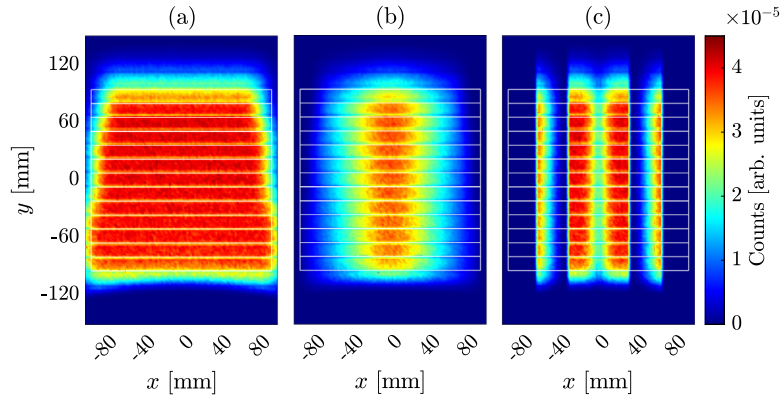


Fig. 6. PSD-picture of the distribution of intensity at the detector position from the simulations (a) without collimation, and (b) and (c) with the analytical and numerical implementations of the collimation, respectively. The 13 squashed tubes dimensions are marked as white rectangles.

the numerical model is important to correctly estimate the detected intensity. This is particularly true for beryllium filters with more complex geometries and non-trivial transmission, for instance with non-parallel Cd blades or with Cd blades with different dimensions, as considered for the TOSCA secondary upgrade. However, the collimation model is not critical to the evaluation of the resolution as the difference in simulated resolutions between the two models is negligible ($<0.2\%$ at the elastic line, $<0.1\%$ at $\hbar\omega = 150$ meV). Note that the inclusion of the collimation itself has but a minor impact on the resolution, which improves by only $\sim 2\%$ at the elastic line and $\sim 1\%$ at $\hbar\omega = 150$ meV compared to the case without collimation. As such, and to facilitate comparisons with the analytical description of the resolution, we selected the analytical model of the collimation in the RT simulations.

The impact of the detector gas tubes is evaluated analytically. A model of stadiums (see Fig. 4(a)) is implemented and the intercept positions of the neutron ray trajectories with the front and back of the stadiums are evaluated. This gives access for each ray to the path length of the neutron in the detector wall and in the ^3He gas. The neutron weights are scaled based on the attenuation by the detector wall, approximated as pure iron with an effective cross section accounting only for the absorption cross section. The neutron rays are then propagated using a Monte Carlo approach with numbers generated from the truncated exponential decay distribution with parameters λ (see Eq. (24)) and d the maximum path length in ^3He as the cut-off distance. Note that this does not include the contribution to the time resolution of the detector from the charge collection and electronics, which unfortunately is expected to be the dominant contribution for the TOSCA squashed tubes.

The detector time resolution can be coarsely approximated by adding to the final TOF a correction in the form of a random number selected from a normal distribution characterised by $\mu = 0$ and σ the estimated time resolution of the detector.

4.3. Data reduction

Neutron rays are then integrated for each detector. To minimise issues with peak fitting we use a thin mesh in TOF of a log base 10 with 10^4 bins per decade. Besides the TOF t , the distributions of E_2 , t_2 , L_1 and L_2 are also calculated. From the mean values of these histogram distributions the TOF is converted to energy transfer using Eq. (4) for each detector.

In a similar fashion as done for the experimental data, the simulated spectra for each detector, and average spectrum, are then fitted with Gaussian and EMG functions to extract the spectral resolution (FWHM and variance). The peak shape is better fitted by a Gaussian function for $\hbar\omega \leq 10$ meV, by an EMG function between 10 and 250 meV, and again by a Gaussian function for $\hbar\omega \geq 250$ meV.

5. Discussion

5.1. Comparison of approaches

We show in Fig. 7(a) the spectral resolution, in the form of the standard deviation divided by the incident energy, as calculated from the analytical method for the ideal TOSCA geometry, i.e. with $Z_{\text{offset}} = 0$, with perfect and infinitely thin PG tiles, and without the correction for the detector time resolution nor time binning. We also show in Fig. 7(a) the individual contributions to the resolution of t , t_2 , L_1 and L_2 . The contribution from the secondary flight path uncertainty dominates the resolution at the elastic line and up to $\hbar\omega \approx 25$ meV. At higher energy transfer, $\hbar\omega > 25$ meV, the main contribution from the resolution is the time uncertainty from the moderator pulse shape. Note that both the contributions from the primary flight path and secondary TOF uncertainties are minor in comparison.

We also report in Fig. 7(a) the spectral resolution as obtained by the numerical method for the ideal TOSCA geometry (magenta circles, marked McStas in Fig. 7(a)). We observe excellent agreement between the spectral resolutions obtained with the analytical and numerical methods over the entire energy range. For comparison, the resolution of a generic inverted crystal analyser spectrometer [21], using the parameters and variances calculated here for TOSCA, is shown as a dotted black line in Fig. 7(a). This early model provides an estimation of the resolution by simply combining the relative errors from the different components of the spectrometer. The resolution it predicts is overestimated, and particularly so at high energy transfer, as it does not account for the specific time- and energy-focusing geometry of TOSCA. Fig. 7(a) also shows the analytical resolution calculated with VISION's model [8], using the parameters and variances calculated here for TOSCA, as a dashed dotted black line. Note that VISION's model is here modified compared to eqn. 21 in Ref. [8] to use the absolute values of the partial derivatives. While it is in better agreement with the numerical method than the model from Ref. [21], the resolution is slightly overestimated at high energy transfer compared to the numerical method and does not account for the "hump" in the energy range 20–100 meV.

We show in Fig. 7(b) a comparison between the spectral resolution, in the form of the standard deviation, as obtained by the numerical methods for the ideal TOSCA geometry and including various corrections: a more realistic detector offset value of $Z_{\text{offset}} = 59$ mm, 2 mm thick instead of infinitely thin PG tiles, and both corrections together. Together, these two corrections lead to an increase of the resolution from $\sigma/E_1 \approx 3.1\%$ to $\sim 3.5\%$ at the elastic line (from $\text{FWHM}/E_1 \approx 7.2\%$ to $\sim 8.3\%$), and from $\sigma/E_1 \approx 0.28\%$ to $\sim 0.38\%$ at $\hbar\omega = 150$ meV (from $\text{FWHM}/E_1 \approx 0.51\%$ to $\sim 0.71\%$).

In more detail, the inclusion of the tile thickness contribution to the simulations increases the uncertainty in the secondary flight path

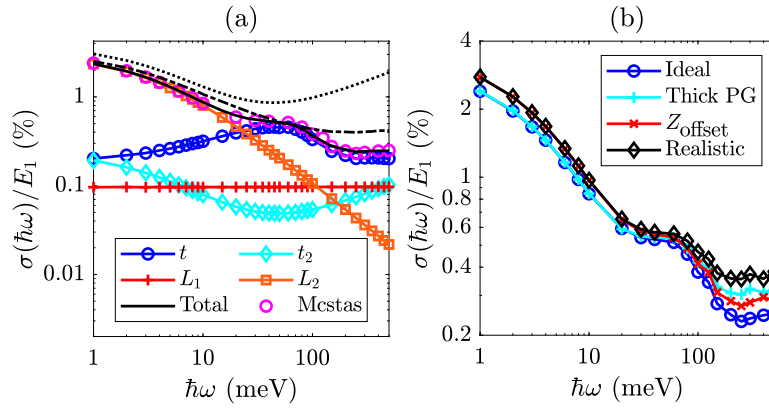


Fig. 7. Spectral resolution in the form of the standard deviation divided by the incident energy in %. (a) Analytical method: individual contributions of t , t_2 , L_1 and L_2 and their sum (black line); numerical method for the same ideal instrument model as the analytical method (magenta circles). The analytical resolutions calculated from the models of Ref. [8] (dashed dotted black line) and Ref. [21] (dotted black line) are also indicated for comparison. (b) Numerical method: ideal model, ideal model with added tile thickness, ideal model with added Z_{offset} , realistic model with both tile thickness and Z_{offset} .

along the propagation direction of the neutron. This has no effect on the resolution at the elastic line since the overall secondary flight path uncertainty is dominated by the widths and heights of the sample and detector, thus the x - and y -directions respectively. It does however degrade the resolution at high energy transfer as the increased secondary flight path uncertainty in the z -direction directly translates into an increased secondary TOF uncertainty. The contribution of the analyser thickness is quantified from the difference between the variances of the two simulations, with and without tile thickness. Using only high energy data points ($\hbar\omega \geq 200$ meV) for which the contribution of t_2 is statistically significant, the average value of the standard deviation from the tile thickness contribution is $2.1(3) \mu\text{s}$. Converted into path length uncertainty, this corresponds to a standard deviation of $1.2(2)$ mm, which is comparable to the value of $2\sigma_{\text{tile}} = 1.4$ mm estimated with NISP for VISION for similar PG tiles [8].

Shifting the detector bank away from the sample plane using Z_{offset} has two effects. The first one comes from the deviation from the ideal time-focusing geometry. Indeed, the neutron energy gradient along the y -direction does not exactly compensate for the variation of flight path anymore for $Z_{\text{offset}} \neq 0$. It follows that the neutrons have slightly different arrival times depending on their point of scattering on the analyser, which broadens the distribution of t_2 and degrades the resolution at high energy transfer. This effect is minor since the neutron front remains essentially uniform for $Z_{\text{offset}} = 59$ mm. The second effect is simply an increased relative error from the decreased value of L_2 and unchanged uncertainties. This is shown in the expression of the squared partial derivative of L_2 (Eq. (23)) when substituting t_2 by its expression in Eq. (6), which gives a dependency of the squared partial derivative in $1/L_2^2$. Similarly, one can show that the squared partial derivative of t_2 (Eq. (21)) is also inversely proportional to L_2 . Consequently, shifting the detector bank towards the analyser leads to a degradation of the spectral resolution over the entire energy range, as it impacts both the secondary flight path and secondary TOF contributions.

Finally, we show in Fig. 8 comparisons between the spectral resolution derived from the experimental data and obtained by the numerical method for the most realistic model (including tile thickness and Z_{offset}), with and without the correction for the detector time resolution. Without this correction, the spectral resolution (FWHM/E_1) is significantly underestimated with a value at high energy transfer of 0.71% instead of $\sim 1.2\%$. The agreement between the experimental and numerical spectral resolutions becomes satisfactory when the detector time resolution is accounted for, using a correction value of $8 \mu\text{s}$ for the detector time resolution. This indicates that the detector time resolution is the limiting contribution to the spectral resolution of TOSCA at high energy transfer. While a correction value of $8 \pm 1 \mu\text{s}$ is consistent with the estimate of $\sim 10 \mu\text{s}$, the exact time resolution of the squashed detector

tubes used on TOSCA is yet to be experimentally determined, which will be the object of future work. Note that the resolution at the elastic line is correctly accounted for in both simulations, as we have shown in Fig. 7(a) that the resolution is dominated by the secondary path length uncertainty at $\hbar\omega = 0$ meV.

Qualitatively, the analytical approach developed here gives similar results to that developed for VISION for a single analyser tile and ideal time-focusing geometry, which is expected given the similarities between the two instruments [8]. In particular, the dependency with energy transfer of the individual contributions to the resolution, as well as their relative intensities, are comparable. As in the present work, the spectral resolution in Ref. [8] is dominated by the secondary flight path uncertainty at the elastic line and at low-energy transfer and by the moderator pulse shape contribution at high-energy transfer. The minor contribution of the primary flight path uncertainty $\sigma(\hbar\omega)$ is also found to be linear with energy transfer. Finally, the minor contributions to $\sigma(\hbar\omega)/E_1$ of the sample, analyser and detector thicknesses exhibit a shallow minimum near $\hbar\omega = 50$ meV, as found for t_2 in the present work. The main differences between the two approaches concern the treatment of the secondary TOF uncertainty. The method developed here predicts smaller values of $V[t_2]$ due to the path length uncertainties in the sample, analyser and detector, as compared to Ref. [8]. Because the detector time resolution contribution turned out to be much larger than the contributions of the sample, tile and detector thicknesses to the experimental spectral resolution of TOSCA at high energy transfer, we cannot discriminate between the two analytical approaches. Indeed, we have shown that the inclusion of a correction for the detector time resolution, not accounted for in Ref. [8], is necessary to account for the experimental resolution.

5.2. Insights into instrument design

From these descriptions of the spectral resolution of TOSCA we obtain several insights into the critical contributions to the instrument performance, which are useful in the context of the proposed upgrade of the TOSCA secondary spectrometer and, in general, for the development of similar instruments.

In the case of the TOSCA secondary upgrade, as the moderator and guide are unchanged, the only contribution relevant to the spectral resolution in the energy range of interest is the uncertainty in the secondary TOF. The design of the upgraded secondary, of the large curved analyser and detector system, thus has to be optimised to minimise the uncertainty in t_2 . We have shown that this uncertainty depends on the analyser geometry and how well it enforces time-focusing. Indeed, we have evidenced the degradation of the spectral resolution when shifting the detector bank away from the sample plane

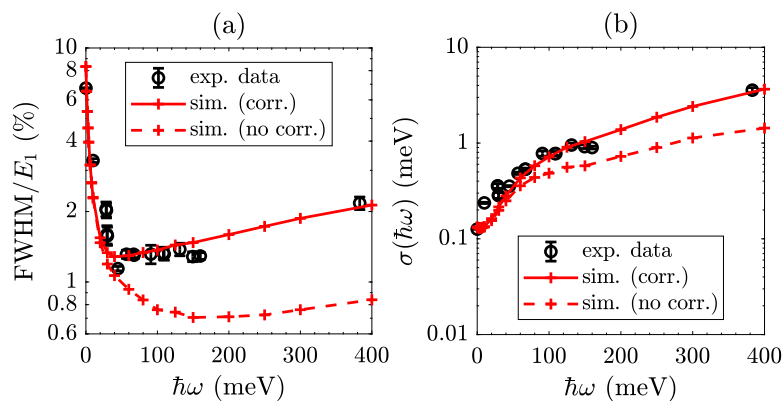


Fig. 8. Comparison between the spectral resolution obtained by fitting the experimental data (black markers) and fitting the numerical simulations for the realistic model with $Z_{\text{offset}} = 59$ mm, 2 mm thick PG tiles, and with (full red lines) and without (dashed red lines) the correction for the detector time resolution. Experimental data and simulations are for the forward detector banks. (a) Full width at half maximum (FWHM) divided by the incident energy in %, and (b) standard deviation in meV.

(Fig. 7(b)). While the effect is minor for the current TOSCA with its flat analyser bank and uniform neutron front, it might become significant when large curved analysers and a design further away from the ideal time-focusing geometry are considered.

The other contributions to the uncertainty in the secondary TOF depend on the experiment-dependent sample thickness, the PG tile thickness, the data acquisition electronics binning scheme and the detector time resolution that encompasses the neutron capture profile in the detector, the charge collection, and the detector electronics. These contributions can be considered intrinsic as they depend on the choice of materials and systems. In particular we have shown that, for TOSCA, the time resolution of the detector system is the limiting contribution to the performance of the instrument in terms of spectral resolution (cf. Fig. 8). While the squashed design of the detector tubes successfully decreases the uncertainty in the distribution of path length in the detector, this benefit is outweighed by the large contribution from the charge collection and electronics. Note that this contribution is not usually included in numerical simulations as it is irrelevant for most instruments, and it is extremely complicated to a priori estimate the detector time resolution of a detector system, especially complex ones. This is, however, a fundamental contribution for instruments like TOSCA and provides us with important requirements for the specifications of the detector system for the prospective upgrade of the TOSCA secondary spectrometer. Indeed, modern PSD ^3He cylindrical detector tubes can exhibit time resolutions close to 1 μs . This provides the opportunity to maintain, or improve, the current resolution despite stepping away from the ideal time-focusing geometry resulting from the use of large and focusing PG analysers as proposed for the TOSCA upgrade.

Another important insight that emerged from the simulations of TOSCA is the importance of the beryllium filter design and, in particular, its built-in collimation. As shown in Fig. 6, accurate modelling of the beryllium filter collimation is critical to the correct estimation of the detected intensity, and thus the prospective gain factors in intensity achievable with the upgrade. Note that the limited transmission of analysed neutrons of about 50% for the current filter leaves a large margin for improvement. With the advances of beryllium machining and shaping techniques, more complex designs of the beryllium filter can be produced and transmission beyond 75% is potentially achievable, thus a least a factor 1.5 in gain factor in intensity. Together with minor improvements of $\sim 10\%$ in detector efficiency and considering an achievable 6-fold increase in solid angle from the use of large and focusing PG analysers, a gain factor in intensity of one order of magnitude is feasible, without degrading the instrument spectral resolution.

6. Conclusions

We have developed analytical and numerical descriptions of the spectral resolution of the broad-band indirect-geometry time-of-flight neutron spectrometer TOSCA. The analytical description is derived by error propagation on the energy transfer equation and implements the expected value and variance notations to account for the neutron distribution profiles in each component of the instrument. The numerical description is based on neutron ray-tracing simulations with the McStas code, operated with an in-house Matlab code that also handles post-processing and data reduction and visualisation. Both descriptions are in excellent agreement for identical models of the instrument and reveal the dependencies of the spectral resolution on the uncertainties in the primary and secondary flight paths and the primary and secondary time-of-flights.

We have evaluated the ideal time-focusing geometry and a more realistic model of the instrument which includes the offset position of the detector bank as well as terms not often included in neutron RT instrument simulations such as the thickness of analyser tiles, the neutron capture profile in the ^3He gas detectors, and a correction for the detector time resolution due to charge collection and electronics. The spectral resolution obtained from the simulation of this realistic model are in excellent agreement with the resolution derived from experimental data and indicate that the limiting contribution to TOSCA resolution at high energy transfer is not the secondary design but the time resolution intrinsic to the detector system.

These descriptions provided several insights into the critical contributions to the instrument performance, directly relevant to the proposed upgrade of TOSCA secondary and in general to other broad-band crystal-analyser spectrometers. In particular, the detail assessment and simulation of the detector system and beryllium filter built-in collimation revealed large margins for improvement of the spectral resolution and gain factors. Together with a large increase of the PG analyser solid angle coverage, a carefully designed beryllium filter and detector system would lead to an upgraded instrument offering a tenfold increase in detected intensity without degrading the instrument resolution.

Declaration of competing interest

The authors declare that they have no known competing financial interests or personal relationships that could have appeared to influence the work reported in this paper.

Data availability

Data will be made available on request.

Acknowledgements

This work was supported by the Science and Technology Facilities Council (STFC), United Kingdom. Discussions with Davide Raspino of the ISIS Detector group and Dr. Robert Bewley are gratefully acknowledged. The author thanks Prof. Stewart F. Parker for proofreading the article.

Appendix A. Supplementary data

Supplementary material related to this article can be found online at <https://doi.org/10.1016/j.nima.2022.167401>.

References

- [1] S. Rudić, A.J. Ramirez-Cuesta, S.F. Parker, F. Fernandez-Alonso, R.S. Pinna, G. Gorini, C.G. Salzmann, S.E. McLain, N.T. Skipper, TOSCA International Beamline Review, STFC RAL Technical Report RAL-TR-2013-015, 2013, <http://dx.doi.org/10.5286/raltr.2013015>.
- [2] L. Lin, A.M. Sheveleva, I. da Silva, C.M.A. Parlett, Z. Tang, Y. Liu, M. Fan, X. Han, J.H. Carter, F. Tuna, E.J.L. McInnes, Y. Cheng, L.L. Daemen, S. Rudić, A.J. Ramirez-Cuesta, C.C. Tang, S. Yang, Quantitative production of butenes from biomass-derived γ -valerolactone catalysed by hetero-atomic MFI zeolite, *Nature Mater.* 19 (2020) 86–93, <http://dx.doi.org/10.1038/s41563-019-0562-6>.
- [3] Y. Ma, W. Lu, X. Han, Y. Chen, I. da Silva, D. Lee, A.M. Sheveleva, Z. Wang, J. Li, W. Li, M. Fan, S. Xu, F. Tuna, E.J.L. McInnes, Y. Cheng, S. Rudić, P. Manuel, M.D. Frogley, A.J. Ramirez-Cuesta, M. Schröder, S. Yang, Direct observation of ammonia storage in UiO-66 incorporating Cu(II) binding sites, *J. Am. Chem. Soc.* 144 (2022) 8624–8632, <http://dx.doi.org/10.1021/jacs.2c00952>.
- [4] K.W.B. Hunvik, P. Loch, L.P. Cavalcanti, K.K. Seljelid, P.M. Rø ren, S. Rudić, D. Wallacher, A. Kirch, K.D. Knudsen, C. Rodrigues Miranda, J. Breu, H.N. Bordallo, J.O. Fossum, CO₂ capture by nickel hydroxide interstratified in the nanolayered space of a synthetic clay mineral, *J. Phys. Chem. C* 124 (2020) 26222–26231, <http://dx.doi.org/10.1021/acs.jpcc.0c07206>.
- [5] M.P.M. Marques, A.L.M. Batista de Carvalho, A.P. Mamede, A. Dopplapudi, S. Rudić, M. Tyagi, V. Garcia Sakai, L.A.E. Batista de Carvalho, A new look into the mode of action of metal-based anticancer drugs, *Molecules* 25 (2020) 246, <http://dx.doi.org/10.3390/molecules25020246>.
- [6] A. Ivanov, M. Jimenez-Ruiz, J. Kulda, IN1-LAGRANGE – The new ILL instrument to explore vibration dynamics of complex materials, *J. Phys. Conf. Ser.* 554 (2014) 012001, <http://dx.doi.org/10.1088/1742-6596/554/1/012001>.
- [7] M. Jimenez-Ruiz, A. Ivanov, S. Fuard, LAGRANGE – The new neutron vibrational spectrometer at the ILL, *J. Phys. Conf. Ser.* 549 (2014) 012004, <http://dx.doi.org/10.1088/1742-6596/549/1/012004>.
- [8] P.A. Seeger, L.L. Daemen, J.Z. Larese, Resolution of VISION, a crystal-analyzer spectrometer, *Nucl. Instrum. Methods Phys. Res. Sect. A* 604 (2009) 719–728, <http://dx.doi.org/10.1016/j.nima.2009.03.204>.
- [9] I. Natkaniec, D. Chudoba, Ł. Hetmańczyk, V.Y. Kazimirov, J. Krawczyk, I.L. Sashin, S. Zalewski, Parameters of the NERA spectrometer for cold and thermal moderators of the IBR-2 pulsed reactor, *J. Phys. Conf. Ser.* 554 (2014) 012002, <http://dx.doi.org/10.1088/1742-6596/554/1/012002>.
- [10] G. Škoro, R. Bewley, S. Lilley, R. Ewings, G. Romanelli, M. Gutmann, R. Smith, S. Rudić, S. Ansell, A tale of two foils: ISIS TS-1 water moderators, *J. Phys. Conf. Ser.* 1021 (2018) 012039, <http://dx.doi.org/10.1088/1742-6596/1021/1/012039>.
- [11] R.S. Pinna, S. Rudić, S.F. Parker, J. Armstrong, M. Zanetti, G. Škoro, S.P. Waller, D. Zacek, C.A. Smith, M.J. Capstick, D.J. McPhail, D.E. Pooley, G.D. Howells, G. Gorini, F. Fernandez-Alonso, The neutron guide upgrade of the TOSCA spectrometer, *Nucl. Instrum. Methods Phys. Res. Sect. A* 896 (2018) 68–74, <http://dx.doi.org/10.1016/j.nima.2018.04.009>.
- [12] A. Perrichon, TOSCA Secondary Spectrometer Upgrade. Part I – Analytical and Monte Carlo Study of the Spectral Resolution of TOSCA, STFC RAL Technical Report RAL-TR-2021-002, 2021, <http://dx.doi.org/10.5286/raltr.2021002>.
- [13] R.S. Pinna, M.J. Rudić, Capstick, D.J. McPhail, D.E. Pooley, G.D. Howells, G. Gorini, F. Fernandez-Alonso, Detailed characterisation of the incident neutron beam on the TOSCA spectrometer, *Nucl. Instrum. Methods Phys. Res. Sect. A* 870 (2017) 79–83, <http://dx.doi.org/10.1016/j.nima.2017.07.018>.
- [14] M. Zanetti, F. Masi, S. Rudić, J. Armstrong, S.F. Parker, F. Fernandez-Alonso, G. Gorini, Crystal analyzers for indirect-geometry broadband neutron spectrometers: Adding reality to idealized design, *J. Synch. Investig.* 14 (2020) S242–S250, <http://dx.doi.org/10.1134/S10274510200070526>.
- [15] R.S. Pinna, S. Rudić, M. Zanetti, D. Zacek, S.F. Parker, G. Gorini, F. Fernandez-Alonso, Monte Carlo Simulations for the TOSCA Secondary Spectrometer Upgrade, STFC RAL Technical Report RAL-TR-2017-013, 2017, <http://dx.doi.org/10.5286/raltr.2017013>.
- [16] K. Lefmann, K. Nielsen, Mcstas, a general software package for neutron ray-tracing simulations, *Neutron News* 10 (1999) 20–23, <http://dx.doi.org/10.1080/10448639908233684>.
- [17] P. Willendrup, E. Farhi, K. Lefmann, McStas 1.7 – A new version of the flexible Monte Carlo neutron scattering package, *Physica B* 350 (2004) E735–E737, <http://dx.doi.org/10.1016/j.physb.2004.03.193>.
- [18] P. Willendrup, E. Farhi, E. Knudsen, U. Filges, K. Lefmann, McStas: Past, present and future, *J. Neutron Res.* 17 (2014) 35–43, <http://dx.doi.org/10.3233/JNR-130004>.
- [19] P.C.H. Mitchell, S.F. Parker, A.J. Ramirez-Cuesta, J. Tomkinson, *Vibrational Spectroscopy with Neutrons*, World Scientific, London, 2005, pp. 67–136, <http://dx.doi.org/10.1142/5628>, Ch. 3, Instrumentation and Experimental Methods.
- [20] S. Ikeda, N. Watanabe, High resolution TOF crystal analyzer spectrometer for large energy transfer incoherent neutron scattering, *Nucl. Instrum. Methods Phys. Res. Sect. A* 221 (1984) 571–576, [http://dx.doi.org/10.1016/0167-5087\(84\)90066-8](http://dx.doi.org/10.1016/0167-5087(84)90066-8).
- [21] C.G. Windsor, *Pulsed Neutron Scattering*, Taylor & Francis, London, 1981, pp. 331–374, Ch. 9, Inverted geometry inelastic spectrometer.
- [22] S.F. Parker, J.L. Parker, M. Jura, Structure and vibrational spectra of 2, 5-diiodothiophene: A model for polythiophene, *J. Phys. Chem. C* 121 (2017) 12636–12642, <http://dx.doi.org/10.1021/acs.jpcc.7b03803>.
- [23] S.F. Parker, F. Fernandez-Alonso, A.J. Ramirez-Cuesta, J. Tomkinson, S. Rudić, R.S. Pinna, G. Gorini, J. Fernández Castañón, Recent and future developments on TOSCA at ISIS, *J. Phys. Conf. Ser.* 554 (2014) 012003, <http://dx.doi.org/10.1088/1742-6596/554/1/012003>.
- [24] R.N. Kacker, J.F. Lawrence, Trapezoidal and triangular distributions for type B evaluation of standard uncertainty, *Metrologia* 44 (2007) 117–127, <http://dx.doi.org/10.1088/0026-1394/44/2/003>.
- [25] F.M. Al-Athari, Estimation of the mean of truncated exponential distribution, *J. Math. Stat.* 4 (2008) 284–288, <http://dx.doi.org/10.3844/jmssp.2008.284.288>.
- [26] J.P. Foley, J.G. Dorsey, A review of the exponentially modified Gaussian (EMG) function: Evaluation and subsequent calculation of universal data, *J. Chromatogr. Sci.* 22 (1984) 40–46, <http://dx.doi.org/10.1093/chromsci/22.1.40>.
- [27] S. Ikeda, J.M. Carpenter, Wide-energy-range, high-resolution measurements of neutron pulse shapes of polyethylene moderators, *Nucl. Instrum. Methods Phys. Res. Sect. A* 239 (1985) 536–544, [http://dx.doi.org/10.1016/0168-9002\(85\)90033-6](http://dx.doi.org/10.1016/0168-9002(85)90033-6).
- [28] P. Willendrup, K. Lefmann, McStas (II): An overview of components, their use, and advice for user contributions, *J. Neutron Res.* 23 (2021) 7–27, <http://dx.doi.org/10.3233/JNR-200186>.